Satellite Observations and Modeling of Meanders in the California Current System off Oregon and Northern California

M. IKEDA[1] AND W. J. EMERY

Department of Oceanography, University of British Columbia, Vancouver, B.C. V6T 1W5, Canada

(Manuscript received 21 February 1984, in final form 14 June 1984)

ABSTRACT

Infrared satellite images from the west coasts of Oregon and northern California are used to identify meander patterns in sea surface temperature which appear as large cold tongues extending offshore. Two relatively long series of images from 1982 and a few examples from 1980 and 1983 demonstrate the evolution of the cold tongues from an initial variety of scales (60–200 km), to the fastest growing waves (110–130 km) and then finally to tongues with longer wavelengths (400 km). This is observed to occur over periods of about three months in summer and fall when the coastal circulation is composed of a southward surface current over a northward undercurrent. The initial shorter scale features are believed to be excited by the interaction between the mean current and the coastal topography. Baroclinic instability associated with the vertical shear between the surface current and the undercurrent is found to be responsible for the growth of the features observed in the satellite imagery. A nonlinear numerical model is used to simulate the evolution of these features in summer/fall including the initial excitation, the growth of the dominant waves and the red cascade to longer wavelengths. In winter or spring when the current no longer reverses with depth but flows north or south respectively, the meanders have scales of about 100–120 km consistent with the horizontal scale of features in the bottom topography.

1. Introduction

Summer infrared satellite images from the west coasts of California and Oregon often contain very pronounced tongues of cold water extending westward from the coast. Bernstein *et al.* (1977) discussed the interpretation of some of these features in terms of *in situ* oceanographic data. They concluded that the surface temperature patterns were expressions of mesoscale circulation features observed in *in situ* data. More recently Kelly (1983) considered a relatively large number of images in the area off northern California in association with the Coastal Ocean Dynamics Experiment (CODE). She also found that infrared surface temperature structure is representative of surface circulation features. In her study surface temperature frontal features coincided with observed currents.

A good example of these infrared temperature features is given in Fig. 1, a satellite image from 1 October 1980 which is generally cloud free from northern California to the northern portion of Vancouver Island. Many westward extending cold tongues with their occasional T-shaped termination are apparent. As discussed in detail in Ikeda *et al.* (1984a) this shape is the expression of a matched pair of counter-rotating eddies, called dipole eddies, which carry the cold water initially seaward and then diverge to form the T shape. These matched eddies were observed in hydrographic data off northern California by Mooers and Robinson (1984) and off Vancouver Island by Thomson (1984). Another large dipole expression can be seen in Fig. 1 in the large tongue off south central Vancouver Island. It is interesting to note that similar shapes can be seen in the much smaller scale features that constitute the general north–south temperature gradient. This suggests that these dipole features are not only components of the mesoscale, expressed by the large cold tongues but are also part of the smaller scale phenomena.

A total of six large tongues can be seen in Fig. 1 with the largest farthest south off northern California. Some smaller scale features appear off northern Oregon and northern Washington. Many of the tongues clearly exhibit vorticity as can be seen, for example, in the northernmost tongues which shows the "comma" shape associated with cyclonic flow. In contrast at the lower right edge of the image a large, apparently anticyclonic feature is suggested by an arm of the southernmost cold tongue.

Off northern Washington and Vancouver Island a series of three separate cold patches can be seen. This series of eddies was observed to form as meanders of the band of cold coastal water in the summer/fall of 1980 (Ikeda *et al.*, 1984a). While linear instability theory failed to properly predict the wavelengths of these features, a four-layer numerical model properly simulated both the growth of these features and their

[1] Present affiliation: Ocean Circulation Division AOL, Bedford Institute of Oceanography, Dartmouth, Nova Scotia, BZY4A2 Canada.

© 1984 American Meteorological Society

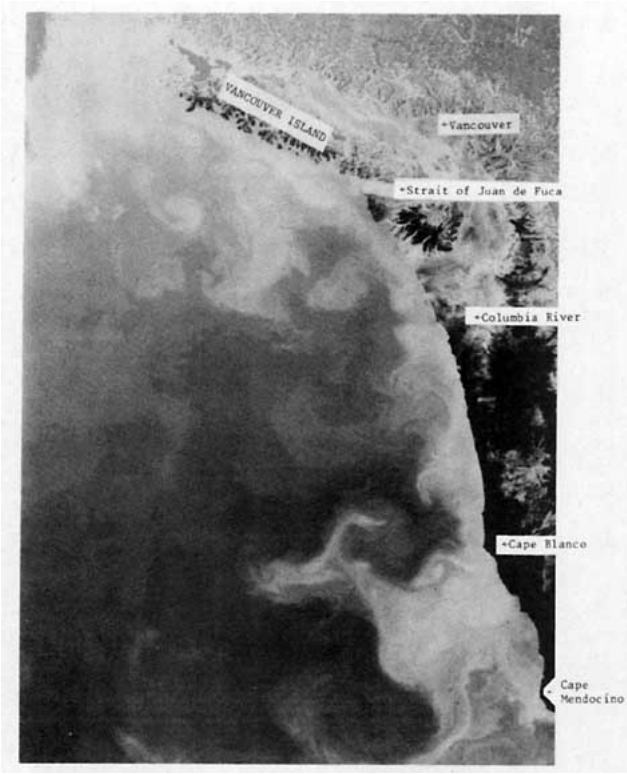

FIG. 1. The satellite infrared image taken by Tiros-N on 2 October 1980. The image covers from Cape Mendocino (lower right) to Vancouver Island (upper left). The brighter color indicates lower surface temperatures.

separation into cyclonic eddies. Subsequent modeling efforts (Ikeda *et al.*, 1984b) revealed that these meanders began as smaller scale (80 km) meanders initiated by an interaction between the current and irregularities in the continental slope. These shorter scale features grew at first and then transferred energy to the 160 km scale first harmonic, which then grew to form the eddy features seen in Fig. 1. It should be noted that subsequent to these studies Thomas (1984) has examined hydrographic data from the coast of Vancouver Island, collected in the summer/fall of 1980, and confirmed not only the existence of the northernmost eddy (Fig. 1) but also its formation through the process of baroclinic instability as demonstrated by the numerical model of Ikeda *et al.* (1984a). It is the purpose of this study to determine the similarities and differences between meanders examined off Vancouver Island and those seen in satellite imagery off northern California and Oregon.

It should be mentioned here that the primary reason for believing that the meanders off California are due to the same mechanism is the similarity in the mean current structure and its seasonal variation. As described by Hickey (1979), and shown schematically in Fig. 2, the summer/fall California Current System is composed of a southward surface current (SC) over a deeper northward undercurrent (CUC). This structure exists somewhat earlier off California as the CUC doesn't extend as far north as Vancouver Island until about May or June each year. In winter this CUC strengthens and surfaces first in the north off Vancouver Island and then later off Oregon and northern California resulting in a northward current in the upper layer (Fig. 2). In spring the entire upper layer flow reverses to flow southward.

This seasonal pattern can also be seen in 1980 current meter records collected off of Vancouver Island, as discussed by Freeland *et al.* (1984). While a north–south phase shift in this current reversal is likely, no long time series of moored current meter measurements were available west of the shelf break off northern California. A short current meter record for the area from April to June 1982 (Beardsley *et al.*, 1983) does show the presence of the CUC beneath a southward flow nearer the surface starting in May.

Off California the SC is strongest in early summer (June, July; Hickey, 1979). The mean summer current profiles used here in the model simulations for both summer and fall pertain to the time before the CUC surfaces to dominate the upper-layer. The midsummer change in the velocity profiles in Fig. 2 reflects the stronger SC in the early summer. It is difficult to estimate mean horizontal current structures with the available data thus currents are taken to have widths of ~50 km as were estimated for the Canadian coast by Ikeda *et al.* (1984a).

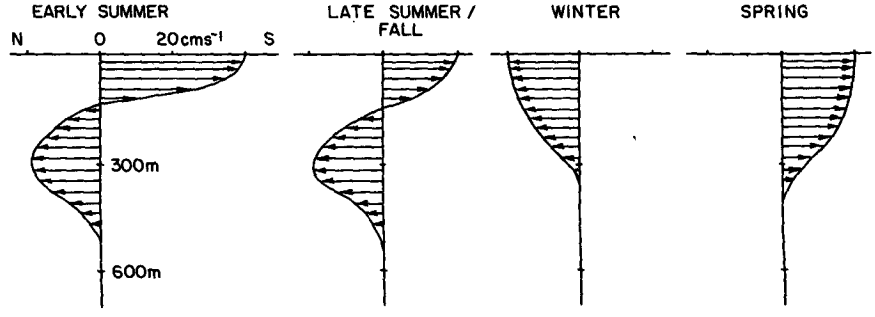

FIG. 2. Seasonal profiles of the meridional California Current off Oregon and northern California (Hickey, 1979).

In summary, the mean vertical current structure for the region west of the continental shelf break off California and Oregon, is assumed to be generally similar to that observed off the west coast of Vancouver Island. Since baroclinic instability has been shown (Ikeda *et al.*, 1984a; Thomson, 1984) to be active in causing the growth of observed meanders off Vancouver Island, the region off California and Oregon is also a likely candidate for baroclinic instability to be contributing to the growth of the very dramatic cold tongues (Fig. 1) seen extending westward from the coasts of California and Oregon.

In what follows, infrared images from the study region are presented and discussed in terms of the meander and eddy features present. Linear stability theory is used to suggest appropriate meander wavelengths for all seasons. Although linear theory suggests that baroclinic instability maintains the growth of the meanders for summer conditions, the observed evolution exhibits a variety of scales rather than the fastest growing wave alone. Hence nonlinear numerical simulations are used, starting with the topographically induced initial meanders, to simulate the meander growth and the subsequent red cascade of meander energy into larger scales. For winter and spring, it is suggested that irregularities in the coastal topography alone are responsible for the observed wavy surface temperature patterns.

2. Infrared Satellite Imagery

Figure 3 serves as reference map for all the images presented in this paper and shows the coastline of northern California and Oregon along with the 200 m isobath. Over the latitudes of interest (37–47°N) this coastline represents an almost meridional boundary with three primary offshore extensions in the bottom topography at 44°N (Heceta Bank), 43°N (Cape Blanco) and 40.5°N (Cape Mendocino). Of these, Cape Mendocino is the largest, corresponding to the Mendocino Ridge which extends far out into the Pacific. The seaward extensions at Cape Blanco and Heceta Bank are much smaller both in east–west and north–south extent. South of Cape Mendocino the coastline turns southeastward deviating from its previous meridional orientation. At 200 m, however, these three bottom topographic features appear, somewhat similar (Fig. 3).

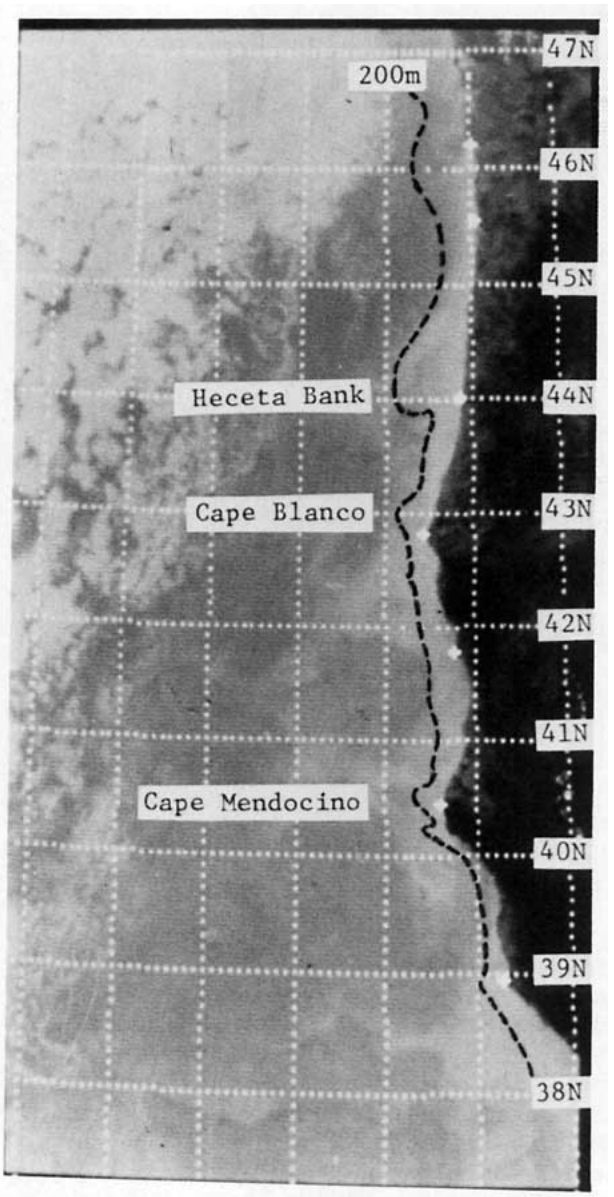

FIG. 3. A reference map including the 200 m isobath between the latitudes of 37 and 47°N.

In the early summer of 1982 a sequence of four satellite images (Fig. 4) documents the evolution of four cold tongues in the area of interest. In these images the dashed line represents the estimated axis of the surface current. In all images light gray shades indicate colder temperatures corresponding to both low cloud and cold sea surface temperatures. In some parts of these images, such as the southwest on 7 June 1982 (Fig. 4b), it is difficult to distinguish between low cloud and the surface tongues of upwelled cold water. However, in most cases the cloud cover was generally to the west of the coastal upwelling region and the cold sea surface tongues could be clearly identified. Initially (28 May) two pronounced tongues of cold water (m3 and m4) extended southward from Capes Blanco and Mendocino, while two weaker tongues (m1 and m2) are seen around Heceta Bank. These two main tongues (m3 and m4) are due to coastal upwelling driven by strong northerly winds over a period of about ten days (prior to 28 May in Fig. 6), which is intensified by the two capes. It should be noted here that the meander events, seen in the satellite image series for 1982, both occur after

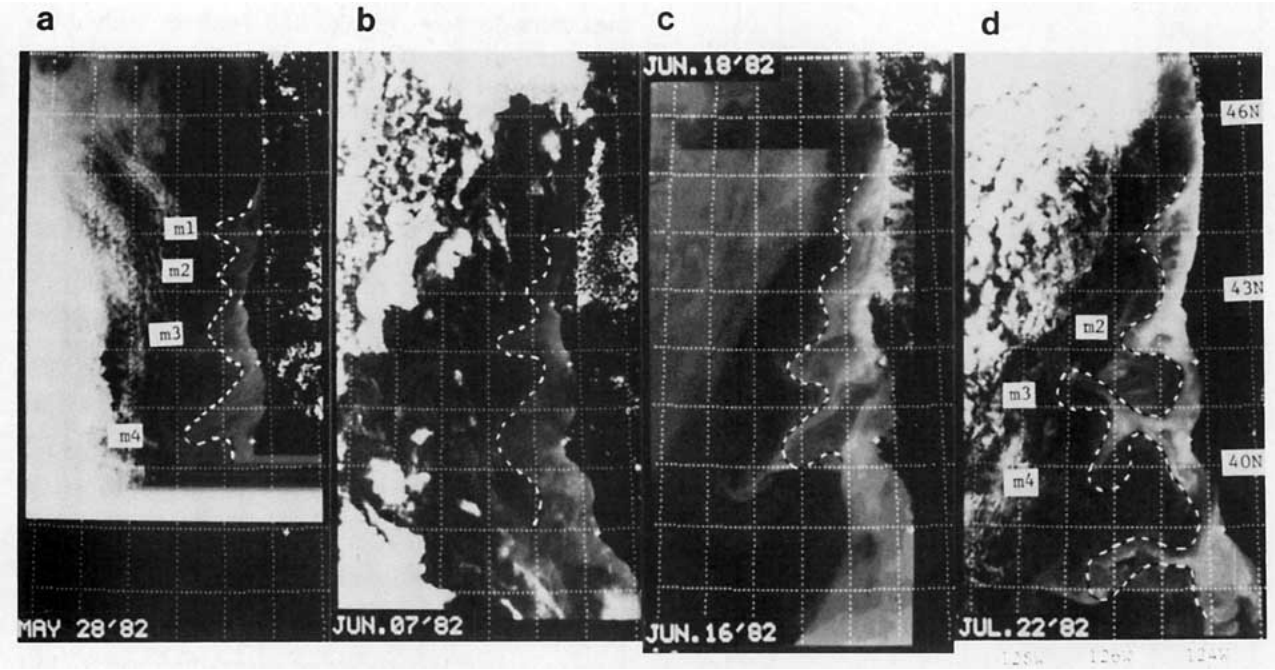

FIG. 4. Enhanced satellite images with estimated surface current axes indicated by dashed lines: (a) 28 May, (b) 7 June, (c) 18 and 16 June and (d) 22 July 1982.

periods of sustained northerly winds favorable for upwelling.

The series starting on 28 May occurs right after a maximum in northerly winds. The wavelength associated with the spacing between m1, m2 and m3 is about 100 km, while m4 is ~200 km from m3. The periodogram of sea surface temperature in Fig. 5a for 28 May is computed from infrared brightness values taken on the line between the two selected points given. It contains a sharp peak at a wavelength of 200 km along with a smaller broad peak around 100 km. While this simple Fourier spectrum of this relatively short spatial series is not statistically significant the prominent peaks in this spectrum emphasize those scales of interest which were subjectively inferred from the individual satellite images. The dominant 200 km peak reflects the spacing of the more pronounced cold tongues. It should be noted that at this initial stage of meander growth both the 100 and 200 km scales could be excited by the bottom topography. Ten days later the image from 7 June (Fig. 4b) suggests the development of a T-shaped expression of a dipole eddy off Cape Blanco.

On 16 June (Fig. 4c) a series of thin ribbon-like tongues can be identified in the infrared pattern. As suggested by the periodogram in Fig. 5b these features have become smaller in horizontal scale. Dominant peaks now occur at 80 and 150 km, similar to the meander scale lengths observed off Vancouver Island in summer/fall (Ikeda *et al.*, 1984a). These narrow tongues have grown considerably in east–west extent compared to 28 May and by 16 June these meanders appear to have propagated south about 50 km in 19 days or about 3 cm s^{-1}. During this time the smaller features farther north appear to propagate faster than the larger scale features in the south reducing the separation between meanders (Fig. 4, 28 May–16 June).

This is even clearer on 22 July (Fig. 4d) when meander m2 overtakes and joins with meander m3. This conjunction of features produces a shift to larger wavelengths as is also suggested by the Fourier spectrum in Fig. 5c. Here the dominant length scale is now 200 km which appears to contain twice the energy of the other wavelengths. Several of the tongues on both 16 June and 22 July terminate in T shapes suggestive of dipole eddies.

A second sequence of meander pattern growth, revealed in the infrared satellite images from 1982, is from 6 August to 13 October (Fig. 7). Again Fig. 6 shows a period of northerly winds prior to this meander growth in the image sequence. Small amplitude meanders once again mark the beginning of the series on 6 August when meanders labelled m1 through m5 can be identified along the west coast. There are again meanders at the three offshore topographic features in addition to others in between. The four meanders, m1, m2, m3 and m5 grow until 18 August, while m4 is absorbed into m3. The Fourier periodogram (Fig. 8a) from 18 August displays a peak at 110 km wavelength which agrees with the scale observed subjectively in the satellite images.

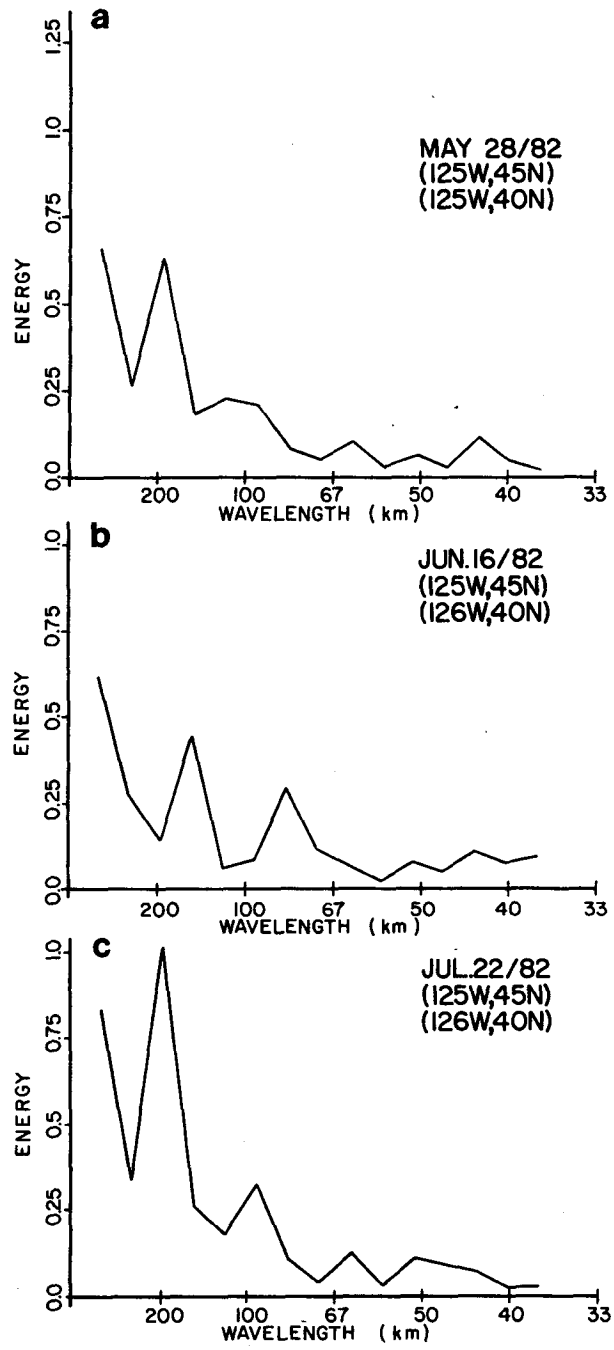

FIG. 5. Periodograms of sea surface thermal data taken on lines between two points designated in the upper right corners for (a) 28 May, (b) 16 June and (c) 22 July.

The small amplitude shorter wavelength features evolve over the next month into three larger scale meanders as shown on 31 August. In contrast to the May–July series these three larger tongues appear more stationary on 31 August which may reflect the expected late summer decrease in southward flow at the surface. Unlike the earlier series the northern meanders do not overtake and coalesce with those farther south; the cold tongues also have a more east–west rather than a southwestward orientation which was apparent in the early summer series.

In September (Fig. 7) these tongues continue to grow extending westward out from the coast over 200 km by 13 September and over 300 km by 13 October. On 31 August (Fig. 7d) there are patches of cold water west of the limit of the three tongues which suggest that cyclonic eddies may have separated from these meanders (It may be that some of these patches may be due to cloud contamination.). This process appears to happen again on 13 September (Fig. 7e) at the central meander and again on 13 October (Fig. 7g) at the far north of the northern tongue. The Fourier spectrum for 13 September (Fig. 8b) again suggests a shift of energy to wavelengths in excess of 200 km. There is another peak in this periodogram at 130 km which indicates the continued presence of the smaller tongues labelled m0 and m6. This second sequence of images demonstrates the cascade of energy from shorter to longer wavelengths. However, a difference is that in the second series the shorter (130 km) scale is not completely replaced and continues to be present.

A similar sequence of images was available for the late summer of 1980 consistent with the period studied by Ikeda *et al.* (1984a) off Vancouver Island. Four of these images are shown in Fig. 9 for the days between 24 August and 8 October. Note that the full image in Fig. 1 is also part of the image series and provides a better description of the surface temperature field than does the final image 6 days later on 8 October (Fig. 9d). As in 1982 the 1980 images reveal initial small amplitude cold meander tongues with relatively short (60 km) wavelengths. On 28 August a somewhat cloud-contaminated image suggests the shift to longer (100 km) wavelengths. The more dramatic shift occurs because of the appearance of larger scale meanders in the composite image from 9 and 12 September in Fig. 9c where features have scales around 200 km. These large-scale tongues grow to form the well developed meander pattern of Fig. 1. Here, and in Fig. 9d (8 October) the dominant wavelength is about 400 km. In 1983 a single fall image from 19 September (Fig. 10) exhibits a wavelength of about 200 km in agreement with the scales in 1980 and 1982 for that phase of the evolution where the meanders have large amplitudes.

In winter the entire upper-layer flow is directed northward (see Fig. 2) and very different length scales dominate the meander pattern. Only a few clear images were available for this season of generally cloudy weather. One example is shown in Fig. 11, an image from 9 December 1982 which shows, although not too clearly, a wavelength of about 120 km in the few cold tongues detected. In spring the upper-layer current reverses to flow southward (see

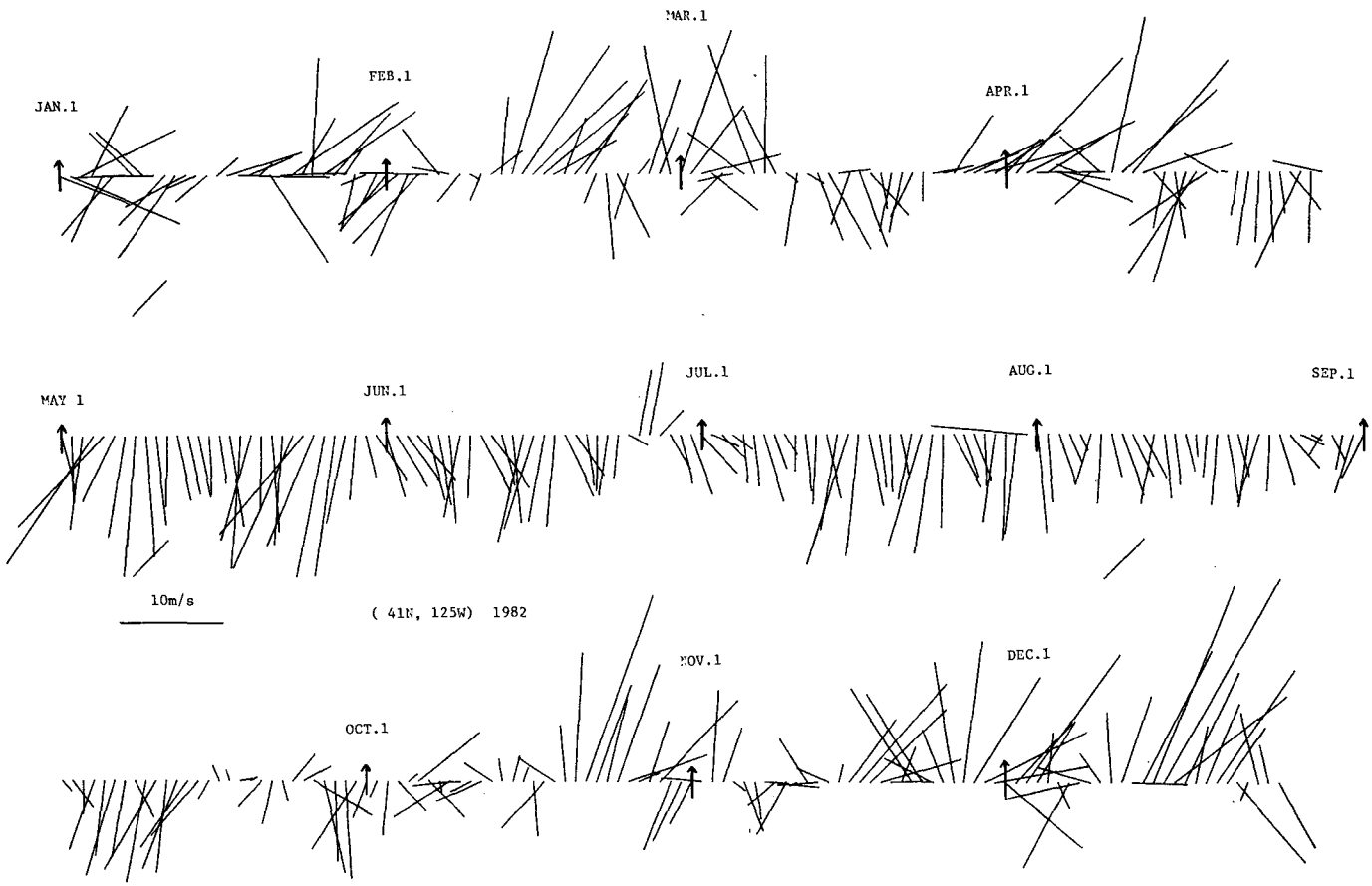

FIG. 6. Wind stick diagram of daily averaged winds at (41°N, 125°W) for 1982.

Fig. 2), and meander length scales are expected to be similar to those in winter. Persistent cloud cover reduced the number of available cloud free images but a sample is shown for 8 April 1982 in Fig. 12. Note that after winter cooling alongshore variations are revealed as a series of warm patches rather than as a series of cold tongues. The wavelength estimated for this pattern of warm patches is 110 km in good agreement with the expected winter length scale of 120 km.

3. Basin model and linear study

a. Modeling

In accordance with Ikeda *et al.* (1984a,b), a four-layer quasi-geostrophic model is used to study the summer and fall meander evolution. The top and second layers contain the southward surface current and northward undercurrent; the relatively motionless lower ocean is divided into two additional layers with different densities. Unlike summer and fall, a three-layer model is employed for winter and spring, because the currents flow northward in winter and southward in spring without an undercurrent and can be represented by a single top layer.

The two models are presented in Fig. 13 with layer thickness, density and cross sections of topography. The thicknesses are estimated from Hickey (1979), and densities are taken from Tabata (1976). The shallow continental shelf is omitted, and the continental slope is modeled by a vertical wall as by Mysak (1977), except for the gentler rise in the middle of the continental slope. This gentle rise has an inclination of 2×10^{-2}.

We choose our horizontal length scale to be the Rossby radius of deformation associated with the top layer in summer,

$$L = \left[\frac{(\rho_2 - \rho_1)gH_1}{\rho_0 f^2}\right]^{1/2} = 15 \text{ km}, \qquad (3.1)$$

where g is the gravitational acceleration, ρ_0 the averaged density, and $f(=10^{-4}\ \text{s}^{-1})$ the Coriolis parameter. All variables are scaled by L (horizontal length), H (total fluid depth as a vertical scale), U (velocity of 20 cm s^{-1}), L/U (time of 0.87 day) and $\rho_j f UL$ (pressure perturbation).

The basic equations used are those expressing the conservation of potential vorticity in an inviscid, quasi-geostrophic flow overlying a gently sloping bottom on a β-plane. The equations for the four-layer model are as follows:

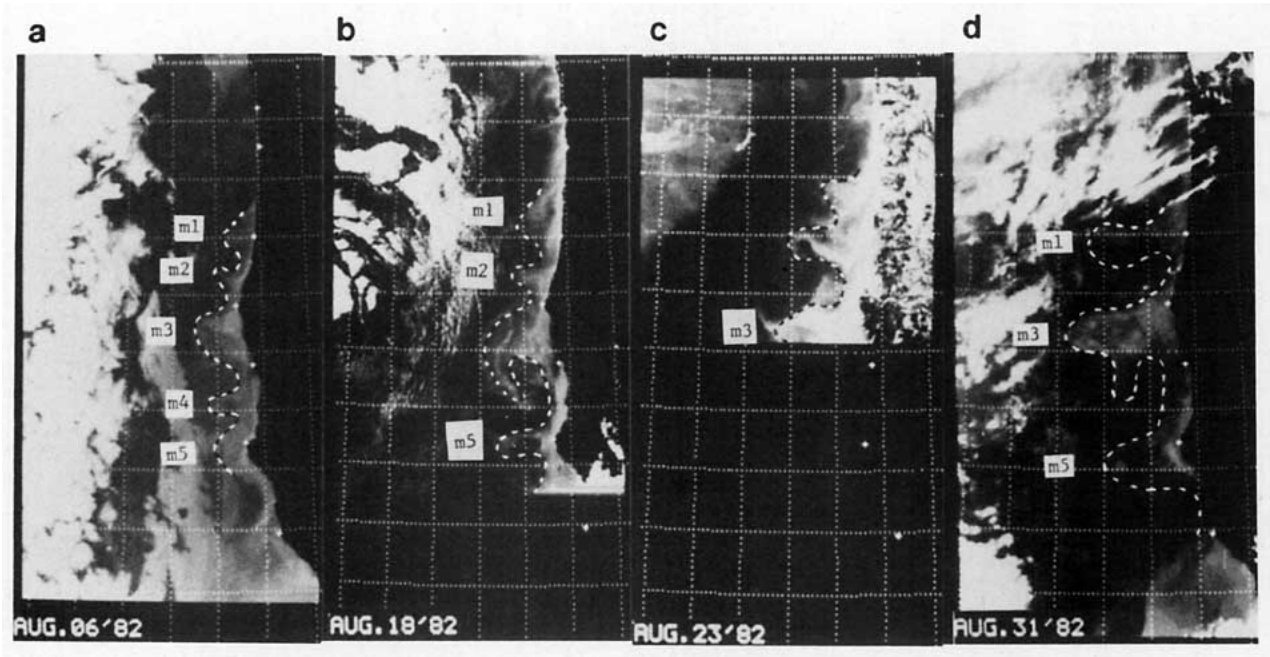

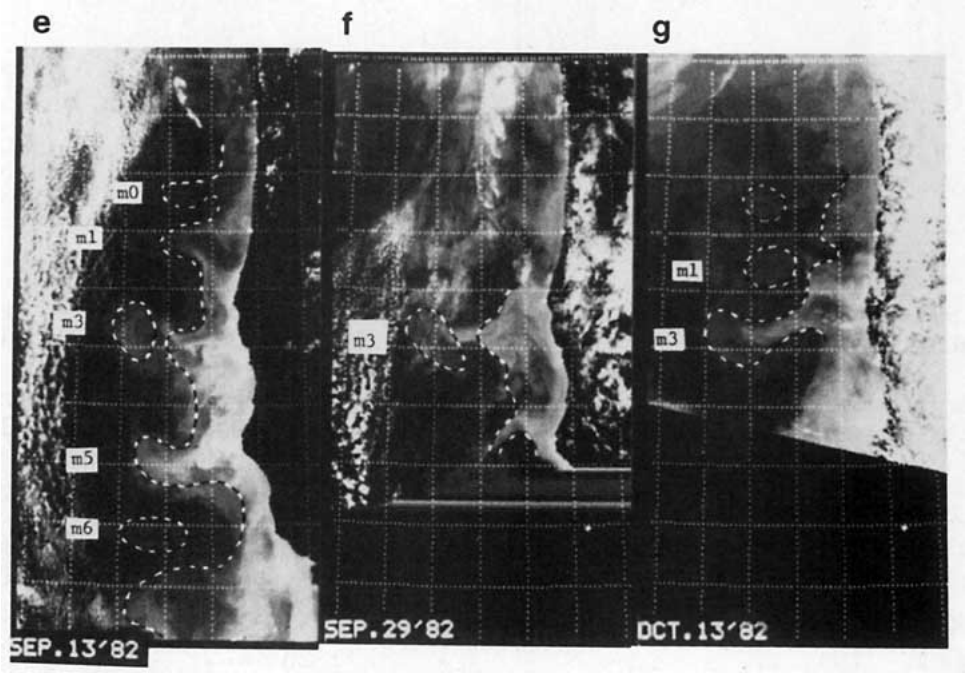

FIG. 7. Satellite images for (a) 6 August, (b) 18 August, (c) 23 August, (d) 31 August, (e) 13 September, (f) 19 September and (g) 13 October 1982.

$$\left.\begin{aligned}
&\frac{D_1}{Dt}\left(\nabla_H^2 p_1 + \frac{F_1(p_2 - p_1)}{d_1} + \beta x\right) = 0 \\
&\frac{D_j}{Dt}\left(\nabla_H^2 p_j + \frac{F_j(p_{j+1} - p_j) - F_{j-1}(p_j - p_{j-1})}{d_j} + \beta x\right) = 0, \quad j = 2, 3 \\
&\frac{D_4}{Dt}\left(\nabla_H^2 p_4 - \frac{F_3(p_4 - p_3)}{d_4} + \beta x\right) = 0
\end{aligned}\right\}, \tag{3.2}$$

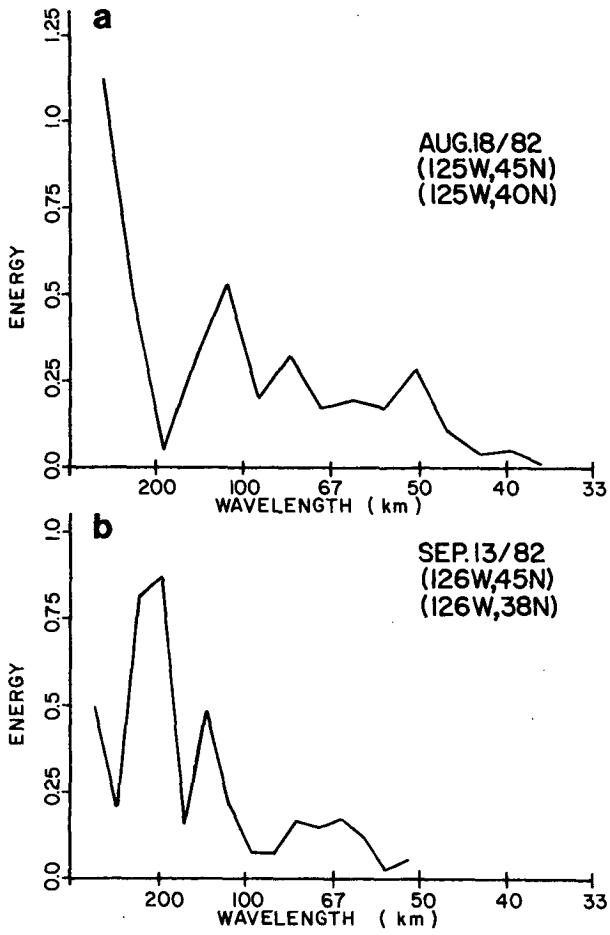

FIG. 8. Periodograms for (a) 18 August and (b) 13 September.

where

$$\left.\begin{aligned} &D_j/D_t = \partial/\partial t + u_j\partial/\partial x + v_j\partial/\partial y, \quad j = 1 \sim 4 \\ &\nabla_H^2 = \partial^2/\partial x^2 + \partial^2/\partial y^2 \\ &(u_j, v_j) = (-\partial p_j/\partial y, \partial p_j/\partial x) \end{aligned}\right\}.$$

The equation for the third layer over the gentle slope is

$$\frac{D_3}{Dt}\left[\nabla_H^2 p_3 + \frac{h - F_2(p_3 - p_2)}{d_3} + \beta x\right] = 0, \quad (3.3)$$

instead of the second equation in (3.2).

The coordinates x and y are chosen to be northward and eastward, respectively, t is time, and p_j denotes the geostrophic streamfunction (i.e., geostrophic pressure). The nondimensional parameters in (3.2) and (3.3) are d_1 $(=H_1/H) = 0.05$, $d_2 = 0.117$, $d_3 = 0.4$, $d_4 = 0.433$, F_1 $(=\rho_0 f^2 L^2/[g(\rho_2 - \rho_1)H]) = 0.05$, $F_2 = 0.1214$, $F_3 = 0.25$, β $(=\beta L^2/U) = 0.018$, where β denotes the meridional variation of the Coriolis parameter. A Rossby number Ro $(=U/fL)$ of 0.13 confirms the validity of the quasi-geostrophic approximation. The sloping topography beneath the third layer, scaled by RoH, is represented by $h = 0.5 - 0.75(y - 2)$.

It is straightforward to reduce (3.2) and (3.3) to the equations for the three-layer model. The parameters change to $d_1 = 0.1$, $d_2 = 0.467$, $d_3 = 0.433$, $F_1 = 0.0773$, and $F_2 = 0.25$.

To represent the summer and fall mean current conditions, the basic flow is given as

$$U_{1B} = U_1\begin{cases}1 - (y/2 - 1)^2, & \text{for } 0 < y < 2 \quad (3.4a)\\ \exp[-(y/2 - 1)^2], & \text{for } 2 < y < 15 \quad (3.4b)\end{cases}$$

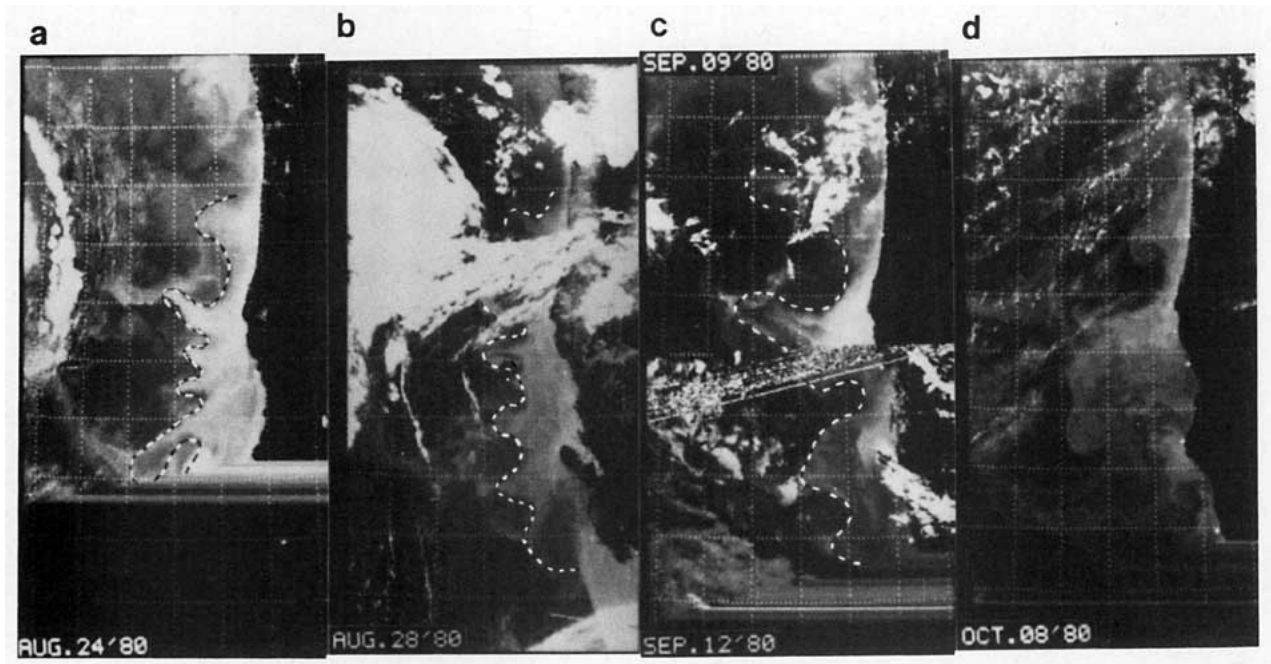

FIG. 9. Satellite images for (a) 24 August, (b) 28 August, (c) 9 and 12 September and (d) 8 October 1980.

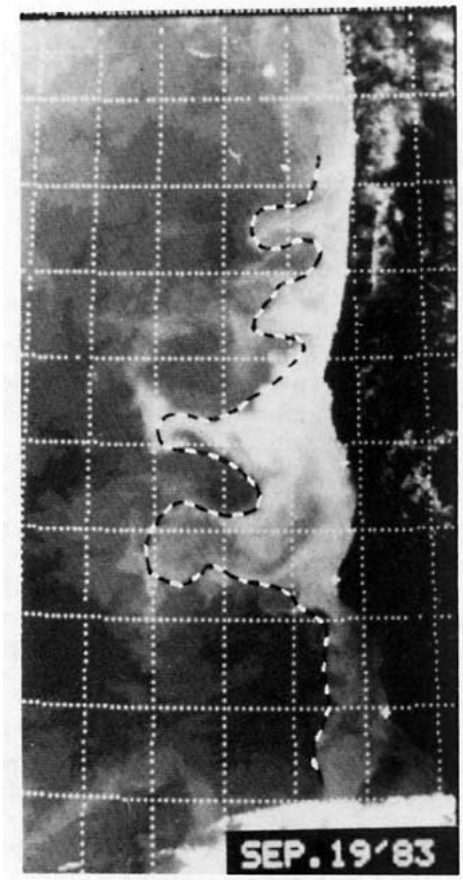

FIG. 10. Satellite image for 19 September 1983.

$$U_{2B} = U_2 \exp[-(y/2 - 2)^2], \quad 0 < y < 15 \qquad (3.4c)$$

$$U_{3B} = U_{4B} = 0.$$

Note that the e-folding half width is 2 (=30 km), the axis of the surface current (U_1) is located at $y = 2$ (=30 km), and the undercurrent axis is at $y = 4$ (=60 km). These model currents are shown schematically along with the idealized coastal topography in Fig. 14. The undercurrent velocity U_2 is fixed to be 1 (20 cm s^{-1} northward), while the surface current velocity U_1 changes seasonally; for example, $U_1 = -2$ for June and July, and $U_1 = -1$ for August and September. The basic flows for winter and spring have $U_1 = 1$ (winter) and $U_1 = -1$ (spring), without the undercurrent ($U_2 = 0$).

b. *Linear stability analysis*

The linear stability analysis is based on the assumption that p_j takes the form of an infinitesimal, travelling wave perturbation of order $\delta \ll 1$ superimposed upon the basic flow; i.e.,

$$p_j = -\int U_{jB} dy + \delta\phi_j(y) e^{ik(x-ct)}. \qquad (3.5)$$

The complex phase velocity c gives a growth rate $\alpha = kc_i$ and a phase speed c_r, where k is a wavenumber, and r and i denote real and imaginary parts. The appropriate boundary conditions and the numerical method used to solve the corresponding eigenvalue problem for ϕ_j are described in Ikeda *et al.* (1984a). Note that the basic flow is reasonably approximated to be steady, because perturbations grow much more quickly than the basic flow changes due to a very small value of β (Kang *et al.*, 1982).

The growth rates, phase velocity and group velocity, based on linear theory, are plotted in Fig. 15. The three summer profiles ($U_1 = -1, -1.5, -2$) lead to fastest growing waves with wavelengths of 120–130 km. These wavelengths are consistent with the meanders which grow fastest in the first ~10 days after their initiation (7 June and 18 August 1982, 28 August 1980). Thus it is suggested that baroclinic instability is responsible for the meander growth during this period. In contrast, the longer wavelengths observed later in each series (22 July and 13 September 1982, 12 September 1980) do not fit with the fastest growing waves. The phase and group velocities greatly depend on U_1; i.e., southward propagation in June and July ($U_1 = -2$), northward propagation in August and September ($U_1 = -1$). This dependency is qualitatively consistent with the meander propagation observed in the satellite images.

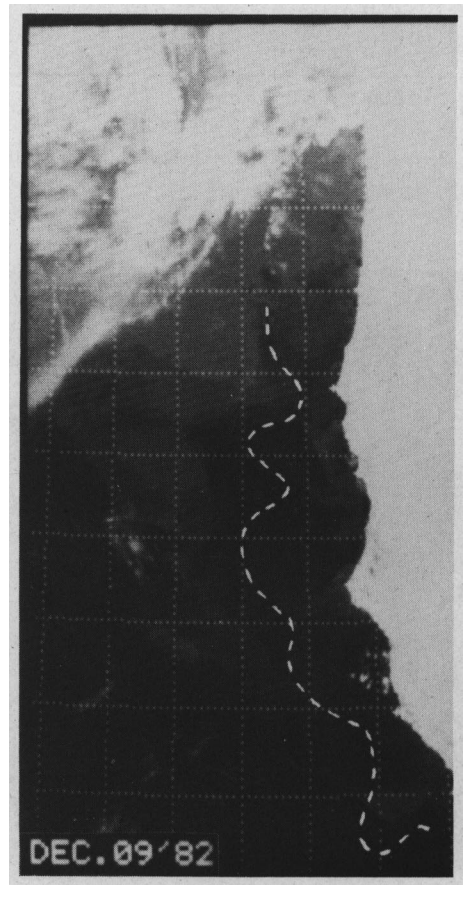

FIG. 11. Satellite image for 9 December 1982.

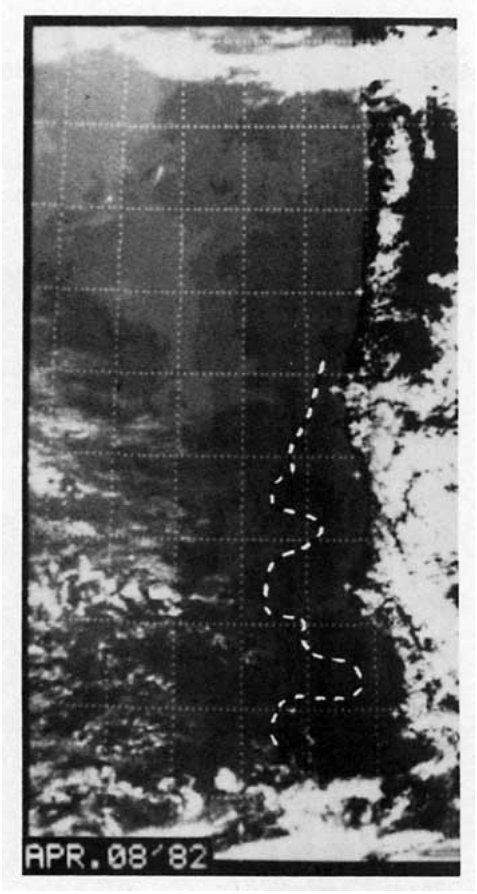

FIG. 12. Satellite image for 8 April 1982.

An energy analysis has been done to examine the sources for the growing perturbations. This analysis suggests that baroclinic instability, due to the vertical shear between the surface current and the undercurrent, is responsible for the rapid growth of the observed meanders in the wavelength range between 100 and 200 km in summer.

The winter and spring mean flows give very slow growth and long (>200 km) wavelengths. Instead of the surface current pattern in Fig. 14, given by Eqs. (3.4a,b), growth rates are computed for the single top-layer basic flows (winter, northward; spring, southward) with the axes more offshore ($y = 4$) but having a symmetric form similar to that shown for the undercurrent in Fig. 14 and specified by Eq. (3.4c). Although the winter/spring model growth rates are longer, even for the cases farther offshore the fastest growing waves have wavelengths of ~200 km. These theoretical results suggest that baroclinic instability is not the mechanism that generates the observed meanders with wavelengths of ~100 km in winter or spring.

4. Nonlinear numerical calculations

a. Modeling of coast line irregularity

As discussed in Section 3, there are observed meanders for which wavelengths are not consistent with the fastest growing waves predicted by the linear theory. Hence, nonlinear calculations in a domain with coastline irregularity are likely needed to simulate the meander evolution and to explain the dynamics.

The three dominant topographic features mentioned earlier are taken into account here; these are, Heceta Bank (44°N), Cape Blanco (43°N) and Cape Mendocino (40.5°N). Note that Heceta Bank is described by the offshore extension of the 200 m isobath, not the coastline. These features are modeled by triangular pillars along the onshore wall as shown in

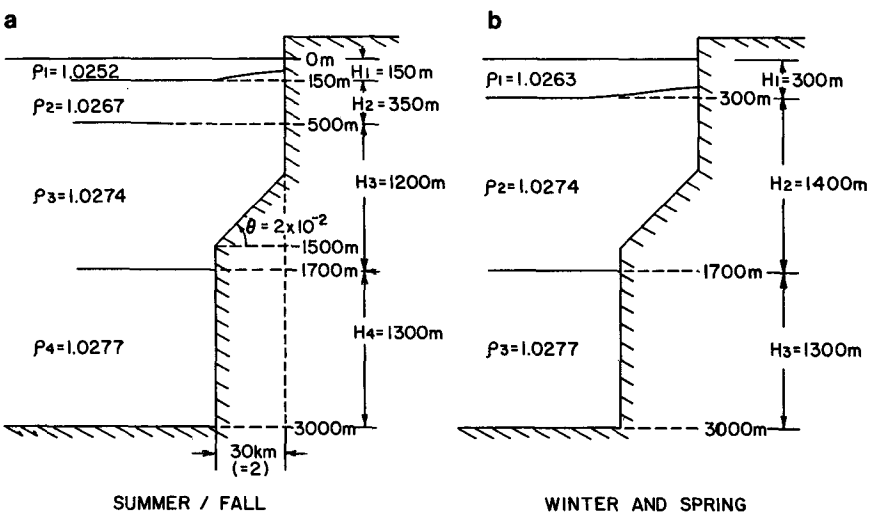

FIG. 13. (a) The four-layer model used to simulate the summer and fall meanders, and (b) the three-layer model for the winter and spring situations. p_j denotes the density in the jth layer, and H_j denotes the thickness.

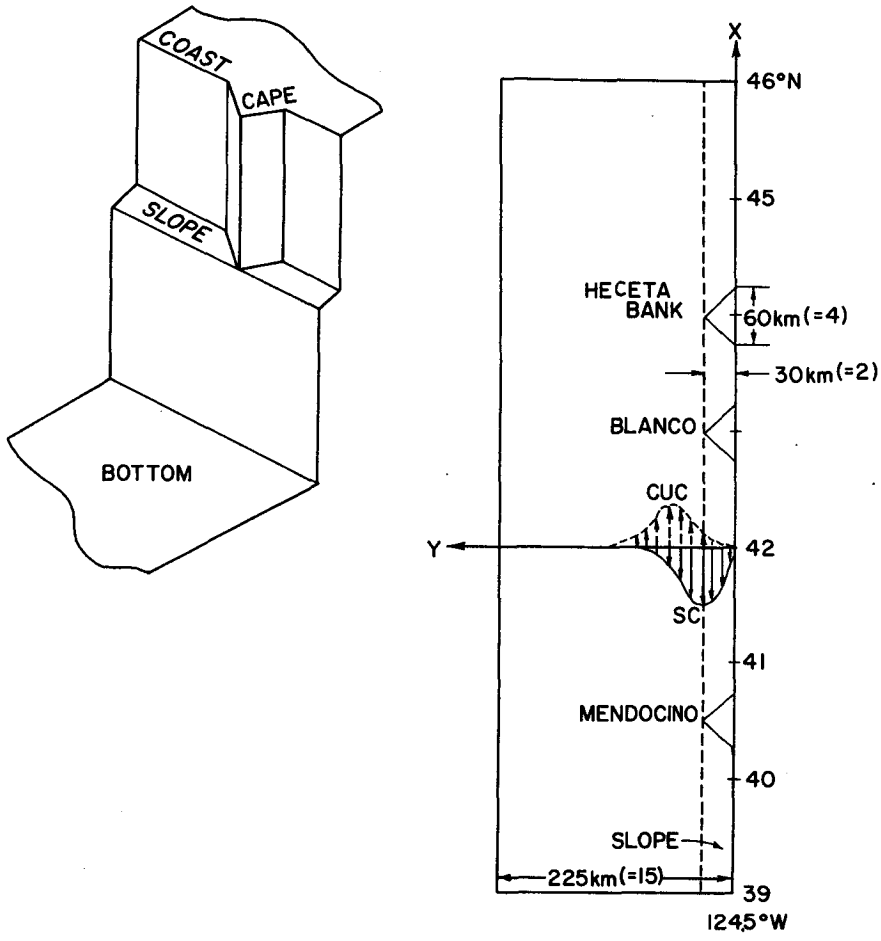

FIG. 14. Shape of the obstacles selected to model the offshore extensions of the coast line or 200 m isobath. The offshore current distributions along with a plan view of the numerical calculation domain.

Fig. 14. The continental shelf, only weakly influences the dynamics (Mysak *et al.*, 1981), and therefore is omitted in this model. Thus it is reasonable to model Heceta Bank by an obstacle reaching the sea surface.

A plan view of the numerical calculation domain also is shown in Fig. 14. The meridional length is 52.5 nondimensional units or 7° latitude (39–46°N), and the zonal width is 15 units (=225 km) with the meridian of 124.5°W as the onshore boundary. The numerical method and periodic boundary conditions are those used by Ikeda *et al.* (1984b). We convert (3.1) and (3.2) to finite-difference equations and integrate them from an initial condition. The integration lattice is square with $\Delta x = \Delta y = 0.25$ (3.75 km). The time step Δt is 0.125 (0.11 day).

b. *Early summer*

The first numerical calculation was performed to simulate the meander evolution observed in June and July 1982 when the surface current is about twice as large as the undercurrent (Hickey, 1979); i.e., $U_1 = -2$ and $U_2 = 1$ (Fig. 2). The model evolution of meanders is presented in Fig. 16 by plotting the streamlines corresponding to the current axes. Initially the surface current (solid line) is taken to have the same shape as the onshore boundary, while the undercurrent (dashed line) is unperturbed. As will be shown, the model results reveal the dominance of the instability scale over the scale of the boundary topography. Thus, it is not likely that the results will be very sensitive to the initial shape of the surface current.

As the calculation time increases up to $t = 10$, meanders of the surface current grow together with undercurrent meanders. Seaward meanders in the surface current are labelled m2–m6 from north to south, where m2, m3 and m5 correspond to meanders at Heceta Bank, Cape Blanco and Cape Mendocino. Meanders m4 and m6 are generated south of Cape Blanco and Cape Mendocino, respectively. Phase velocities of these meanders are ~ 3.5 cm s^{-1} southward, calculated from the southward motion of m2 (30 km) within $t = 10$ (8.7 days). It is not surprising

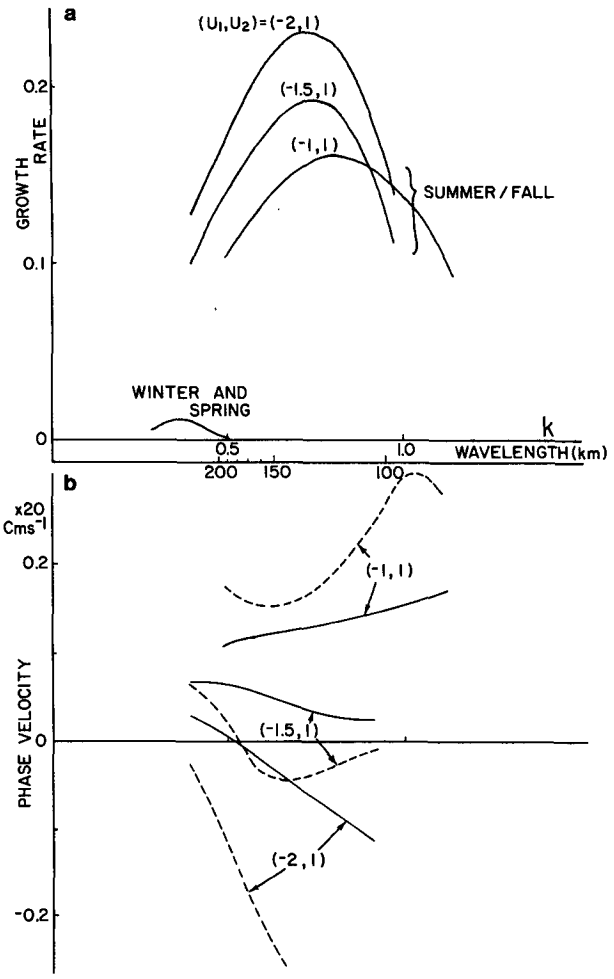

FIG. 15. (a) Growth rates and (b) phase (solid) and group (dashed) velocities with the change in U_1. U_2 is fixed to be 1 for summer and fall. Note that there is no undercurrent for winter and spring ($U_2 = 0$).

that this value is different from the 2 cm s^{-1} for the linear case (Fig. 13), because the initial perturbation is not identical to the linear solution.

The perturbation structures at $t = 10$ are similar to those of the linear solution (not shown); the phase of the perturbation in the top layer shifts northward relative to the second layer. This phase shift implies baroclinic instability in a system with a southward surface current and a northward undercurrent. Thus the meanders which are initiated by the coastal topography grow due to baroclinic instability associated with the shear between the surface current and the undercurrent.

In contrast to monotonic meander growth up to $t = 10$, dramatic changes in the meander pattern occur after $t = 10$. The meander m4 pinches off a weak cyclonic eddy, which is absorbed into m3 by $t = 20$. The meander m3 turns into a strong cyclonic eddy, while m2 propagates faster than m3 and almost overtakes it. To the north of Heceta Bank, another meander m1 grows to be comparable in amplitude to the others. Changing from six seaward meanders at $t = 10$, the resultant streamlines now have three offshore extensions (m1, m3, m5) at $t = 20$. This evolution is confirmed by the model energy spectra of the Fourier components shown in Fig. 17. The components with wavenumbers of 6 and 8 in the domain are dominant until $t = 15$, while the wavenumber 3 and 4 components become more energetic at $t = 20$.

These nonlinear calculations successfully simulate some of the essential characteristics of the observed meander evolutions; e.g., the 110 km wavelength meanders off Cape Blanco on May 28 (Fig. 4a) grow until 7 June (Fig. 4b) and change into the 200 km wavelength meanders by 16 June (Fig. 4c). A similar meander evolution can be seen in Fig. 16 where m3 grows from $t = 0$ to $t = 10$ (~28 May–7 June) while it shifts southward (to the right in Fig. 16). Between $t = 10$ and $t = 20$ the model m3 perturbation has grown shedding a cyclonic eddy. This appears to be happening in the image from 22 July (Fig. 4c). Meander m2 overtakes m3 on a time scale similar to that between 16 June and 22 July. This is also seen in the model results but on a somewhat shorter time scale. The southward model phase velocity of 3.5 cm s^{-1} is close to the observed value of 3 cm s^{-1}. Thus while it is not possible to specifically simulate the individual events seen in the satellite images, the model behavior does suggest the same sequence of meander evolution with similar wavelengths and phase speeds.

In contrast to these similarities, we can see a difference in the periodograms for the initial states; i.e., a 200 km peak from the satellite image on 28 May is not represented by the numerical solutions even up to $t = 10$ (8.7 days). As discussed earlier, this length scale appears to be the result of the combination of the two main cold tongues corresponding to Cape Blanco and Cape Mendocino; in the satellite images, Heceta Bank seems to have a weaker influence in that a cold tongue is not always present. However, for simplicity these three topographic features are modeled by similar-shaped coastal features (Fig. 14), along which the initial streamlines are taken to flow. In addition to dominant modes with wavenumbers 6 and 8, the model initial state has a peak corresponding to wavenumber 2 with a wavelength of 385 km (3.5 degrees) instead of the wavenumber 2.8 component with a 275 km (2.5 degrees) wavelength. In spite of this initial difference, the 110–130 km meanders come to be dominant in the first ten days both in the ocean and the model.

c. *Late summer and fall*

In August, the surface current reduces its velocity to the same magnitude as the undercurrent (Hickey,

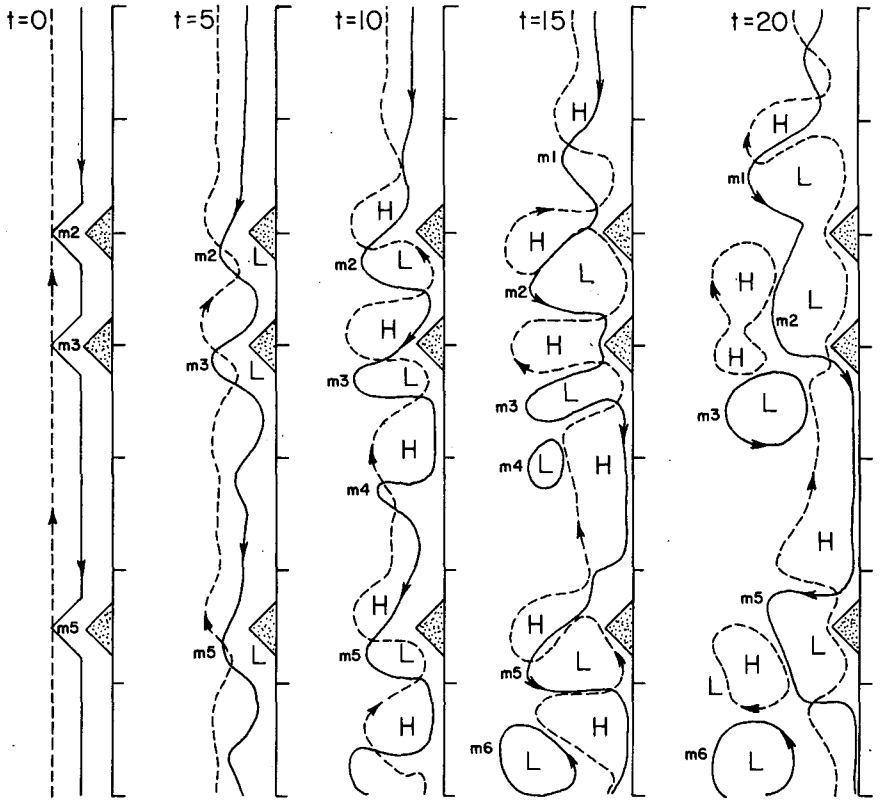

FIG. 16. Time variations of the streamfunctions $p_1 = 0$ (solid) and $P_2 = 0$ (dashed), corresponding to the surface current and undercurrent axes for the first summer/fall event ($U_1 = -2$, $U_2 = 1$). The vertical line with three triangles denotes the onshore boundary. L and H denote a minimum of p_1 and a maximum of p_2, respectively.

1979); i.e., $U_1 = -1$ and $U_2 = 1$ (see Fig. 2). Model runs for this change in the velocity structure yield the current axes plotted in Fig. 18 which describe meander growth similar to that in early summer (Fig. 16). Also shown are some important differences. The phase velocity is now ~ 1 cm s^{-1} northward and the meanders grow slower, increasing monotonically until $t = 20$. These differences can be predicted from the linear theory alone (Fig. 15).

After $t = 20$, the meanders experience, in part, the same evolution as in early summer. As in early summer, six seaward meanders at $t = 20$ evolve into three large-amplitude meanders or detached eddies by $t = 30$. The weak meander m4 is pinched off and absorbed into m3. In contrast to these features common to both late and early summer, m2 does not overtake m3 but turns into a weak eddy by $t = 30$ and remains stationary between m1 and m3.

The general characteristics of the meander evolution observed in satellite images from late summer/fall are again well simulated in the numerical solution. The meanders are nearly stationary in terms of alongshore propagation. Small-amplitude meanders with a shorter ($\sim$110 km) wavelength on 6 and 18 August 1982 (Fig. 7a, b) grow first and then are replaced by large-amplitude, longer ($\sim$200 km) wavelength meanders by 13 September (Fig. 7e). On 13 September weaker meanders, as represented by m0 and m6, remain between the stronger meanders rather than overtaking the southern meanders, while m2 overtakes m3 in early summer (Fig. 4d).

The complete streamfunctions are shown in Fig. 19 for $t = 30$. The cyclonic meanders and detached eddies in the top layer are accompanied by anticyclonic cells on their northern sides; that is, m1 with V1, and so on. The anticyclonic cells are stronger in the second layer. These matched eddy pairs, called dipole eddies (Ikeda *et al.*, 1984a), are again manifested by T-shapes in the satellite images (Figs. 4c, d). The dipole eddies carry cold water seaward due to the offshore velocity imparted by the oppositely rotating cells.

d. Winter

In this section, we examine how meanders are generated in winter, when the California Current possesses only northward flow in the upper 300 m; i.e., $U_1 = 1$. As mentioned earlier, a three-layer model is employed with an initial current in the top layer

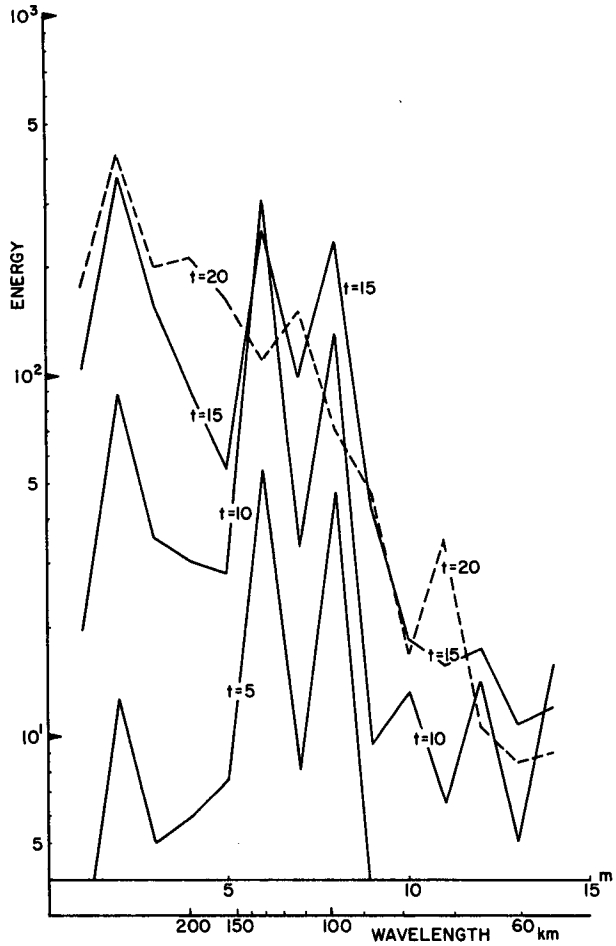

FIG. 17. Time variations of the Fourier component energies (the sum of kinetic and potential energies) for the first summer/fall event as functions of wavenumber m in the calculation domain.

only. Although results will not be shown for spring ($U_1 = -1$), it can be predicted that the meander pattern should be similar to winter only reversed meridionally with respect to the coastal topography. Thus in spring meanders should propagate southward while in winter they move to the north.

Only a single-model streamfunction plot at $t = 30$ is presented for winter (Fig. 20). The meanders m3 and m4 have been initiated by the three main coastal topographic features. The meander pair, m2 and m4, has a wavelength of ~120 km, m5 is separated from m4 by ~180 km. The phase velocity is ~4.5 cm s^{-1} northward. These results suggest that travelling meanders may be generated along the coast even between Cape Blanco and Cape Mendocino. The shapes of the streamlines are similar to the observed current axis (Fig. 11).

5. Discussion

A series of infrared satellite images exhibits mesoscale meanders in the California Current System manifested as sequences of offshore extending cold tongues off Oregon and northern California. Linear stability theory and nonlinear numerical calculations are used to simulate the observed evolutions of these meander patterns and to explain their underlying dynamics.

In summer and fall when the northward undercurrent opposes the surface current, the coastal topography represented by Heceta Bank, and Capes Blanco and Mendocino initiates meanders in a wavelength range between 60 and 200 km. From this range the 110–130 km meanders grow fastest due to baroclinic instability associated with the vertical shear between the surface current and the undercurrent, and are replaced a month later, by longer (~200 km) wavelength meanders through nonlinear wave–wave interactions. Cold cyclonic eddies separate from these longer-scale meanders, accompanied by anticyclonic rotations on their northern sides. There are some differences between early summer and late summer/fall; meanders propagate southward at ~3 cm s^{-1} in early summer, but are nearly stationary in late summer/fall. Northern meanders overtaking those farther south are observed in early summer only. This difference between early and late summer is attributed to the faster surface current present in early summer.

In winter only northward upper ocean flow exists, and meanders, having a wavelength of ~120 km, are generated solely by the coastal topography. Baroclinic instability does not appear to be responsible for the observed meander generation in this case. Since the upper layer current reverses direction in spring, the meander patterns are simply reversed relative to winter.

The meanders off Oregon and northern California have the following similarities to, and differences from, their counter-parts off Vancouver Island: in both areas for summer and fall, the alongshore irregularities in topography initiate meanders with scales similar to the topographic scales. These meanders grow due to baroclinic instability, and experience nonlinear interactions whereby they are replaced by meanders with wavelengths nearly twice as long as the initial meanders. Cold cyclonic eddies finally separate from the longer scale meanders.

In contrast to these common features in summer and fall, the generation mechanisms are different for winter and spring. The coastal topography generates the observed meander patterns along the Washington–Oregon coast, while the ~150 km meanders grow due to baroclinic instability without any relationship to the topography off Vancouver Island. This difference may be due to the fact that topographic irregularity off Vancouver Island is significant only at a depth of ~500 m, where the current is very weak in these seasons.

In the numerical calculations of this study, three major topographic features, Heceta Bank, Cape Blanco

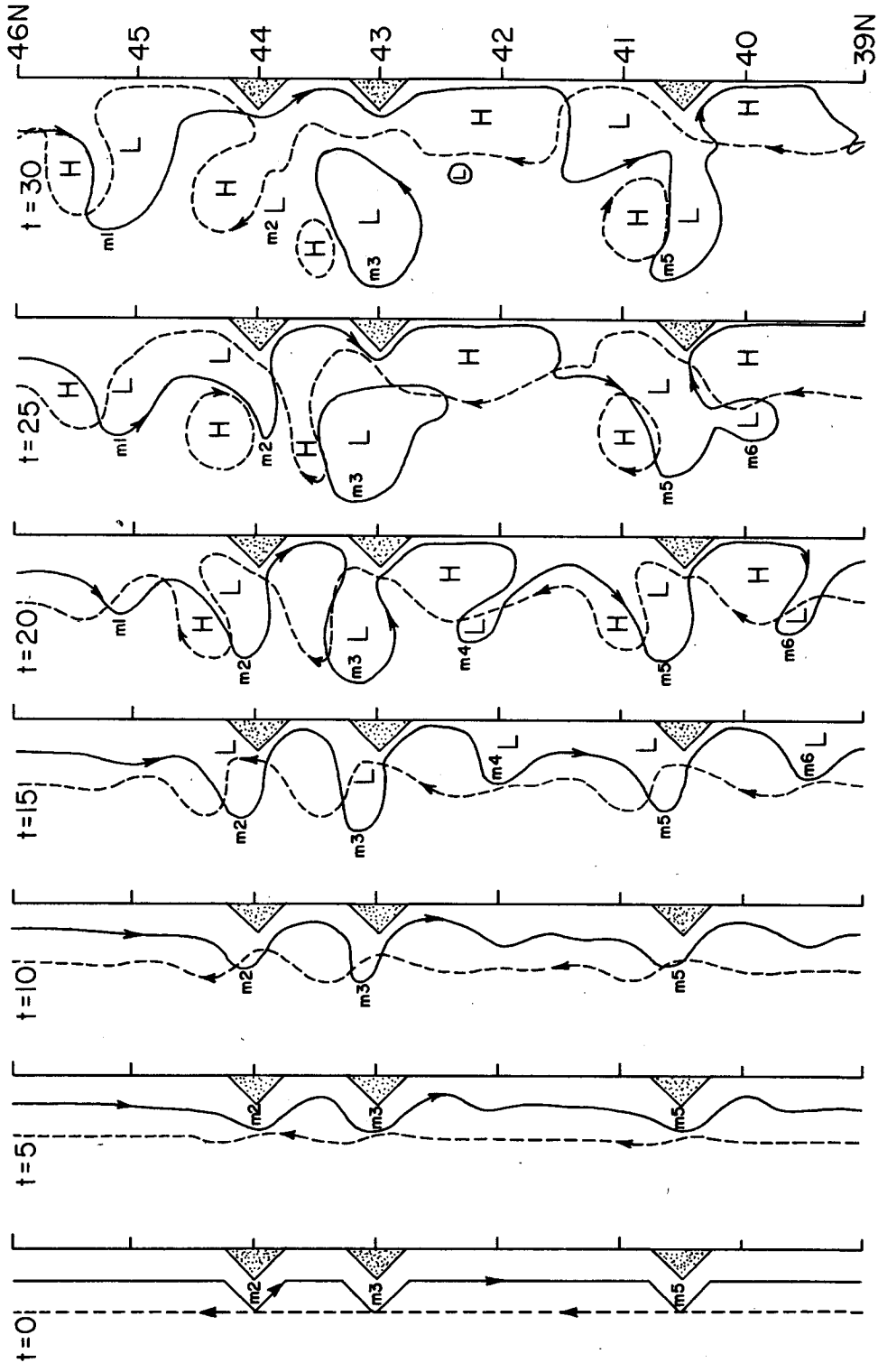

FIG. 18. As in Fig. 16, except for the second summer/fall event ($U_1 = -1$, $U_2 = 1$).

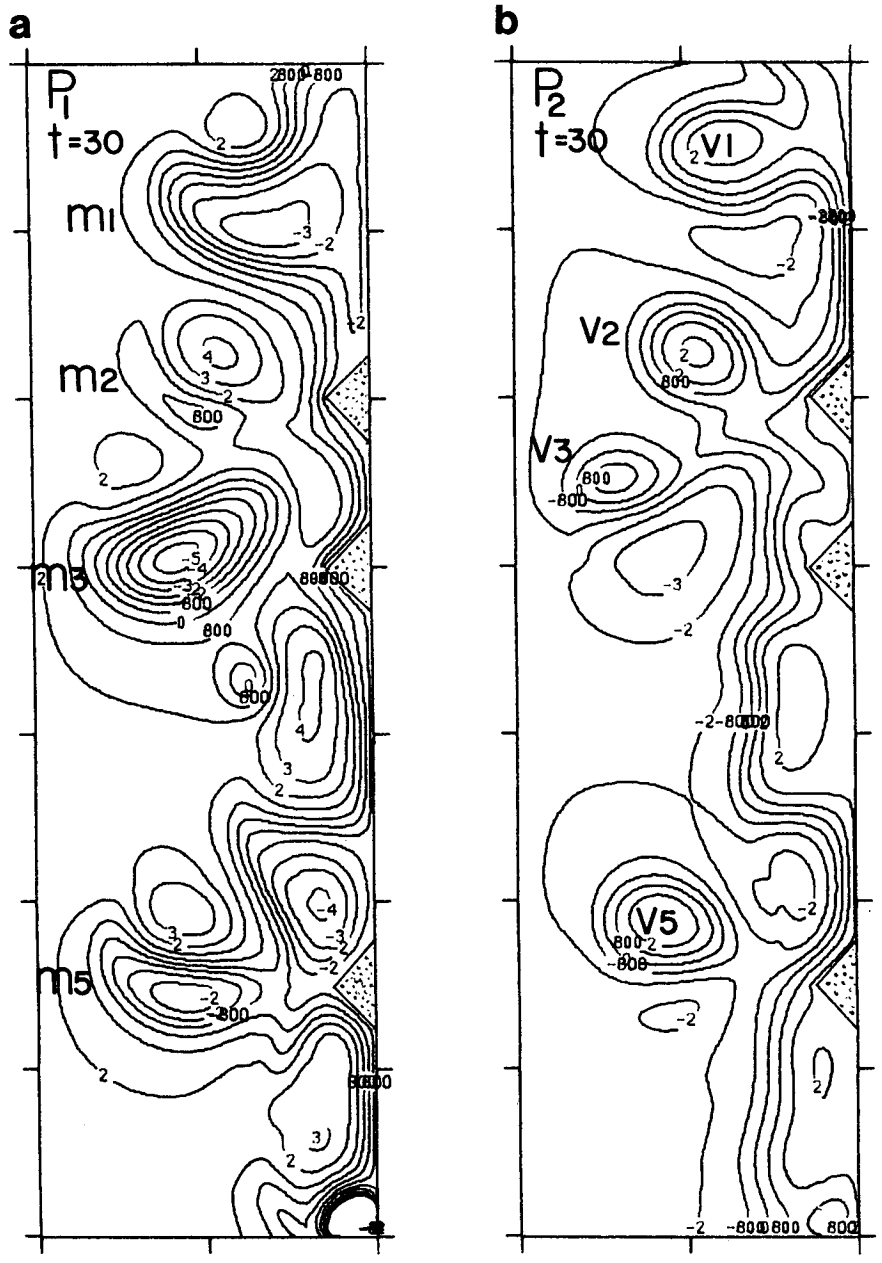

FIG. 19. The full streamfunctions at $t = 30$ for the second summer/fall event. (a) p_1 in the top layer and (b) p_2 in the second layer.

and Cape Mendocino, are modeled by the similar shaped obstacles. There are, however, differences in the actual shapes of these topographic features; that is, Heceta Bank is not reflected by the coast line, and Cape Mendocino continues offshore as a major submarine ridge at a depth of ~1500 m. Heceta Bank may have less influence on the initial offshore extensions of cold tongues than the other capes (Figs. 4a and 7a). The deep topography off Cape Mendocino may also contribute to meander growth. Thus it is unlikely that any of these results will apply to the region south of and around Cape Mendocino where the interaction between the flow and the steep bottom slope should dominate current variations. Our instability model applies most correctly to the region north of Cape Mendocino. The favorable comparison between infrared satellite imagery and the model results was found primarily for this region north of Cape Mendocino. Also with the added complexities of the bottom topography it is not surprising that the ob-

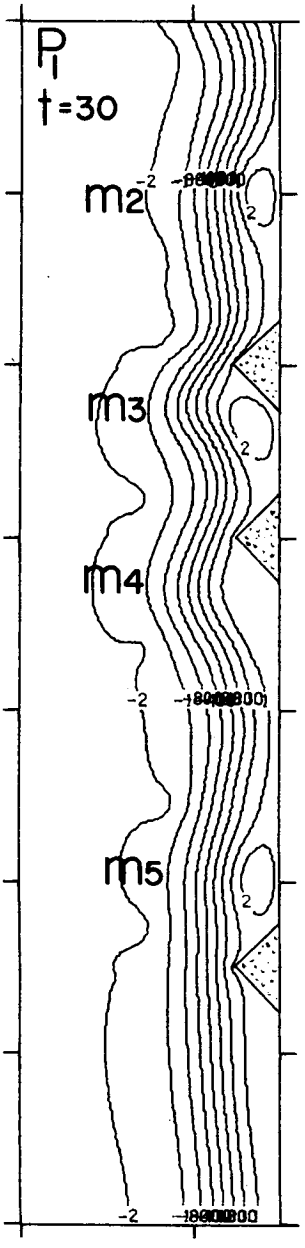

FIG. 20. Streamfunctions in the top layer at $t = 30$ for the winter situation.

served initial meanders are more varied than those in the numerical calculations.

Acknowledgments. The authors wish to thank R. Thomson of the Institute of Ocean Sciences, B.C. for access to his preprint and K. Barber for typing the manuscript. The digital images were supplied by the Edmonton Weather Centre of the Atmospheric Environmental Service, and the 1983 data were received through the antenna operated by P. Nowlan at the University of British Columbia. This research was supported by Strategic Grants to L. A. Mysak and W. J. Emery from the Canadian Natural Sciences and Engineering Research Council. One of the authors (M.I.) worked as a Research Associate with much appreciation of scientific discussion with L. A. Mysak.

REFERENCES

Beardsley, R. C., C. A. Mills and L. K. Rosenfeld, 1983: CODE-1: Moored array and large-scale data report. WHOI Tech. Rep. 83-23, CODE Tech. Rep. No. 21, L. K. Rosenfeld, Ed.

Bernstein, R. L., L. Breaker and R. Whirtner, 1977: California Current eddy formation: Ship, air and satellite results. *Science,* **195,** 353–359.

Freeland, H. J., W. R. Crawford and R. E. Thomson, 1984: Currents along the Pacific coast of Canada. *Atmos. Ocean,* (in press).

Hickey, B. M. 1979: The California Current System—hypothesis and facts. *Progress in Oceanography,* Vol. 8, Pergamon, 191–279.

Ikeda, M., L. A. Mysak and W. J. Emery, 1984a: Observation and modeling of satellite-sensed meanders and eddies off Vancouver Island. *J. Phys. Oceanogr.,* **14,** 3–21.

——, W. J. Emery and L. A. Mysak, 1984b: Seasonal variability in meanders of the California Current System Off Vancouver Island. *J. Geophys. Res.,* **89,** 3487–3505.

Kang, Y. Q., J. M. Price and L. Magaard, 1982: On stable and unstable Rossby waves in non-zonal oceanic shear flow. *J. Phys. Oceanogr.,* **12,** 528–527.

Kelly, K. A., 1983: Swirls and plumes or application of statistical methods of satellite-derived sea surface temperatures, CODE Tech. Rep. No. 18, SIO Ref. 83-15, Scripps Inst. Oceanogr.

Mooers, C. N. K., and A. R. Robinson, 1984: Turbulent jets and eddies in the California Current and inferred cross-shore transports. *Science,* **223,** 51–53.

Mysak, L. A., 1977: On the stability of the California Undercurrent off Vancouver Island. *J. Phys. Oceanogr.,* **7,** 904–917.

——, E. R. Johnson and W. W. Hsieh, 1981: Baroclinic and barotropic instabilities of coastal current. *J. Phys. Oceanogr.,* **11,** 209–230.

Tabata, S., 1976: The general circulation of the Pacific Ocean and a brief account of the oceanographic structure of the North Pacific Ocean. Part II—Thermal regime and influence on the climate. *Atmosphere,* **14,** 1–27.

Thomson, R. E., 1984: A cyclonic eddy over the continental margin of Vancouver Island: Evidence for dynamical instability. *J. Phys. Oceanogr.,* **14,** 1326–1348.